Experimental Comparison of On-Off and All-On Calibration Modes for Beam-Steering Performance of mmWave Phased Array Antenna-in-Package

Gao, Huaqiang; Wang, Weiming; Wu, Yongle ; Liu, Yuanan; Pedersen, Gert Frølund; Fan, Wei

Published in:
I E E E Transactions on Instrumentation and Measurement

DOI (link to publication from Publisher):
10.1109/TIM.2021.3053968

Publication date:
2021

Document Version
Accepted author manuscript, peer reviewed version

Experimental Comparison of On-Off and All-On Calibration Modes for Beam-Steering Performance of mmWave Phased Array Antenna-in-Package

Huaqiang Gao, Weimin Wang, Yongle Wu, Yuanan Liu, Gert Frølund Pedersen, and Wei Fan

***Abstract*—Antenna-in-package (AiP) technology has been implemented for millimeter-wave (mmWave) phased array design with antenna elements and radio frequency (RF) chips integrated. The radiation pattern beam of mmWave phased array AiP is typically steered after the in-homogeneous RF branches are aligned (i.e. AiP calibration). The RF branch discrepancies among elements are directly obtained with one element enabled sequentially each time (i.e. on-off mode) by default in the industry. A recent study has reported that the AiP element branch discrepancies obtained in the on-off mode might be different from those obtained in the normal all-on working mode with all elements active. However, experimental results that demonstrate the impact of difference between the two calibration modes on the beam-steering performance of mmWave phased array AiP have been rarely reported in the literature. In this paper, the beam-steering performance of two mmWave AiPs after the two calibration modes is experimentally compared, which is demonstrated by the beam-steering pattern defined in the paper. Following the statement on the source of difference between the two calibration modes of AiP, the system model is described for the calibration and beam-steering measurements of AiP in the experimental campaign. Experimental results show that the on-off calibration mode obtains the same beam-steering performance as the all-on mode for the main beam pattern, though element branch discrepancies obtained in the two modes are different.**

***Index Terms*—Millimeter-wave (mmWave) antenna-in-package (AiP), phased array calibration, beam-steering, antenna measurement, radio frequency integrated circuits.**

I. Introduction

PHASED arrays in millimeter-wave (mmWave) frequency bands are being widely employed in different applications such as 5G radios [1]–[3], automotive radars [4]–[6], and satellite communication [7]–[9]. The electronic beam-steering is the key capability of mmWave phased arrays, e.g. to establish the optimum link between mobile terminal and base station with beams aligned in 5G cellular networks [10], and to detect objects in automotive radars [11]. As an antenna and packaging technology for various mmWave applications, antenna-in-package (AiP) technology integrates antenna elements and radio frequency (RF) chips into a package for the mmWave phased array design [12]–[16], i.e. mmWave phased array AiP (AiP for short in the following). In practical AiP systems, the initial complex excitation of AiP element might differ from each other due to the imbalances among RF branches of AiP elements. The beam-steering performance (e.g. beam-steering direction and beam pattern) of AiP would be distorted if the RF branches are misaligned, i.e. without AiP calibration. The objective of AiP calibration is to first obtain the initial complex excitation discrepancies among elements and then to compensate for the element-to-element discrepancies, i.e. to make the RF branches of elements aligned. On the basis of the aligned RF branches, beam-steering is performed by extra phase shift settings of elements in AiP. Therefore, the beam-steering performance of AiP is guaranteed by the AiP calibration.

In practice, the initial excitation of elements is never known since the element ports are not accessible. To estimate the initial excitation discrepancies among elements, phased array calibration methods reported in the literature can be adopted for AiP calibration. The estimate of the initial excitation discrepancies among elements can be performed in the near field and far field. As a direct strategy adopted in the industry (i.e. near-field scanning probe method [17]–[19]), a probe antenna is placed in front of each element one by one using a positioner in the near field of AiP, which requires accurate mechanical positioning and precise knowledge of the AiP antenna configuration. In the far field case, the probe antenna is typically placed in the broadside direction of AiP where the excitation discrepancies among elements can be measured in two modes, i.e. on-off mode [20]–[22] and all-on mode [23]–[25]. In the on-off mode, one element is enabled sequentially each time, while all elements are enabled in the all-on mode. A recent study has shown that the element-to-element discrepancies obtained in the two modes might be different in a practical AiP [26]. Since the beam-steering operation of AiP normally works in the all-on mode, the element-to-element discrepancies obtained in the all-on mode is naturally chosen as the ground-truth of element discrepancies in the normal working mode.

This work was supported by the Key-Area Research and Development Program of Guangdong Province, China (2019B010157001), the National Natural Science Foundation of China (No. 61821001), and the Beijing Natural Science Foundation (No. JQ19018). (Corresponding author: Weimin Wang and Wei Fan.)

Huaqiang Gao is with the Beijing Key Laboratory of Work Safety Intelligent Monitoring, Department of Electronic Engineering, Beijing University of Posts and Telecommunications, Beijing 100876, China, and also with the Antenna Propagation and Millimeter-wave Systems (APMS) section, Department of Electronic Systems, Faculty of Engineering and Science, Aalborg University, Aalborg 9220, Denmark (e-mail: gaohq@ieee.org).

Weimin Wang, Yongle Wu, and Yuanan Liu are with the Beijing Key Laboratory of Work Safety Intelligent Monitoring, Department of Electronic Engineering, Beijing University of Posts and Telecommunications, Beijing 100876, China (e-mail: wangwm@bupt.edu.cn; wuyongle138@gmail.com; yuliu@bupt.edu.cn).

Gert Frølund Pedersen and Wei Fan are with the Antenna Propagation and Millimeter-wave Systems (APMS) section, Department of Electronic Systems, Faculty of Engineering and Science, Aalborg University, Aalborg 9220, Denmark (e-mail: gfp@es.aau.dk; wfa@es.aau.dk).

However, obtaining the element discrepancies is only the first step of AiP calibration. The final objective of AiP calibration is to compensate for the element discrepancies and perform beam-steering. Although the element discrepancies obtained in the two modes might be different, it is not yet clear whether the compensation for the element discrepancies measured in the traditional on-off mode leads to different beam-steering performances of AiP in the normal all-on working mode compared with the compensation for those measured in the all-on mode. Adopted for the phased array calibration in sub-6 GHz, the traditional on-off calibration mode has been directly applied to the AiP in the industry. Therefore, it would be desirable to validate the applicability of traditional on-off calibration mode for the beam-steering performance of AiP in the all-on working mode by investigating the beam-steering performance difference between the two calibration modes. Very few contributions have been reported on this study in the literature.

In this paper, an experimental comparison of the AiP on-off and all-on calibration modes is investigated for the beam-steering performance. A beam-steering pattern is defined in the paper to demonstrate the beam-steering performance of an electronically-steered AiP. The defined beam-steering pattern records the change of radiation pattern in the broadside direction of AiP when the radiation pattern is electronically steered towards different directions. The experimental results of AiP beam-steering patterns using the two calibration modes are compared. Finally conclusions are given based on the experimental comparison.

II. Problem Statement

In this section, the source of difference between the on-off and all-on calibration modes of AiP is discussed in terms of the obtained element discrepancies. As shown in Fig. 1 under a far-field plane wave assumption, a probe antenna is located in the broadside direction of AiP to measure the element field vector (i.e. amplitude and phase) over the air. Assuming the free-space propagation scenario, the measured field vector E_n of the n-th element can be expressed as

$$E_n = a_n \cdot g_n \cdot G \cdot \frac{\lambda \exp(-jkR)}{4\pi R}, \tag{1}$$

where a_n and g_n are the initial complex excitation and the complex pattern in the broadside direction of AiP for the n-th element, respectively. G denotes the probe pattern in the broadside direction of AiP. The free-space propagation coefficient is expressed by the fractional term where λ, $k = 2\pi/\lambda$, and R are the wavelength, the wave number, and the far-field propagation distance, respectively.

In conventional conducted testing with element ports accessible, the element excitation a_n is measured directly. However, the element pattern is inherently included in the over-the-air (OTA) testing where it is not possible to de-embed the unknown element pattern. Therefore, in practice, the element pattern discrepancies in the broadside direction of AiP is included in the measured element field vector discrepancies among elements. Defining the product of a_n and g_n as the composite excitation $c_n = a_n g_n$ for the n-th element, the measured element field vector discrepancies generally indicate the composite excitation discrepancies among elements, which can be obtained in the on-off and all-on modes of AiP.

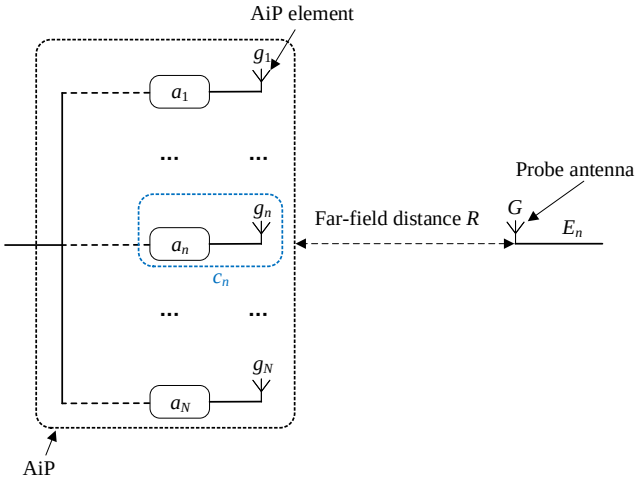

Fig. 1. Illustration of AiP calibration in the far field.

Unlike the phased array design in sub-6 GHz, the AiP is an active device integrating antenna elements and other RF components (e.g. power amplifiers, attenuators, phase shifters, power dividers, and switches, etc.). Depending on the AiP design, the AiP condition in the on-off and all-on modes might be different in terms of device temperature and element coupling. The AiP temperature in the two modes is typically different unless the temperature is properly controlled. The amplifier output can be changed due to the variation of AiP temperature, which brings the variation of element initial excitation a_n. On the other hand, the element coupling in the two modes can be considered as the same on the condition that the disabled elements are terminated by matched loads in the on-off mode of AiP. However, this condition is typically unknown since the AiP is a "black-box" design with all RF components integrated into a package. Several situations are possible for the others when one element is enabled in the on-off mode, e.g. attenuated, powered off by amplifier, matched, etc. For this reason, the coupling effect is not necessarily the same in the two modes, which might change the element pattern g_n. Therefore, the measured composite excitation discrepancies among elements (i.e. element-to-element discrepancies) can be different due to the variation of AiP temperature and element coupling in the two modes.

III. System Model

In this section, the system model of experiment is described for the measurement campaign later. The experimental system diagram is shown in Fig. 2 where the far-field plane wave assumption has to be met in the following descriptions. The AiP is an $L \times L$ uniform rectangular array (URA) with an element spacing d. A probe antenna is located in the broadside direction of AiP for the far-field OTA measurements of AiP, i.e. calibration and beam-steering measurements in the paper. The scattering transmission parameter S between AiP feed and probe antenna feed is recorded by a vector network analyzer

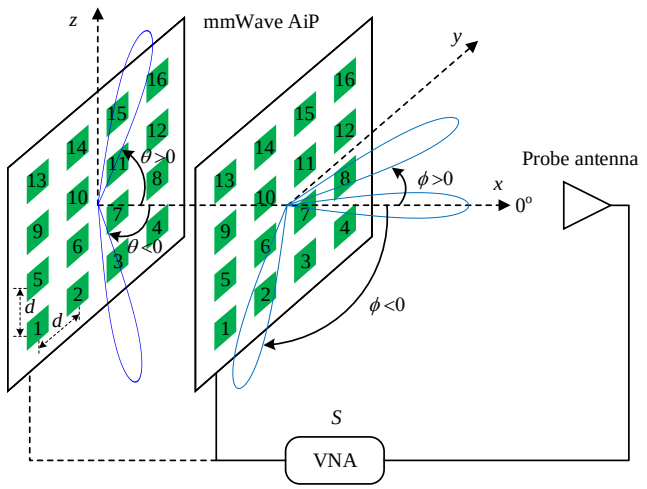

Fig. 2. Diagram of experimental system in the measurement campaign ($L = 4$ for example).

(VNA) for the measurements. In the calibration measurement, element excitation discrepancies are first obtained by the recorded S and then compensated for in AiP. For the beam-steering measurement of the electronically-steered AiP, the available phase shifts of elements are simultaneously set in AiP to electronically steer the radiation pattern beam accordingly. The recorded S varying with the beam-steering angle of radiation pattern is defined as the beam-steering pattern in the paper, which tracks the change of AiP radiation pattern in the broadside direction when the radiation pattern is electronically steered to different angles.

A. Calibration Mode

As mentioned in Section II, the AiP calibration is first to obtain the discrepancies of composite excitation c_n among $N = L \times L$ elements. The excitation discrepancies among elements obtained in the on-off and all-on modes are briefly reviewed below.

1) On-Off: In the on-off calibration mode, N measurements of S are conducted for N elements. For S_n in the n-th measurement, the n-th element is enabled while the others are off. Assuming the AiP feed signal F, we have,

$$S_n = \frac{E_n}{F}. \tag{2}$$

Relative to the first element, the excitation discrepancy coefficient α_n of the n-th element can be obtained by

$$\frac{S_n}{S_1} = \frac{E_n}{E_1} = \frac{c_n}{c_1} = \alpha_n. \tag{3}$$

2) All-On: Taking the well-known rotating element electric field vector method [23] for example in the all-on calibration mode, multiple measurements of S are conducted for each element. When all elements are enabled in an initial state, the phase shift of the n-th element is set from 0° to 360° with a uniform minimal step $\mu = 360°/2^K$ (K is the bit number of phase shifters). One S measurement is conducted for each phase shift setting. Based on the $2^K + 1$ measurements of S for the n-th element, a complex coefficient P_n is obtained as (detailed in [27])

$$P_n = \frac{E_n}{E_0}, \tag{4}$$

where $E_0 = \sum_{n=1}^{N} E_n$ is the total field vector of N elements in the initial state. Hence, the excitation discrepancy coefficient α_n of the n-th element relative to the first element in the all-on mode can be obtained by

$$\frac{P_n}{P_1} = \frac{E_n}{E_1} = \frac{c_n}{c_1} = \alpha_n. \tag{5}$$

After obtaining the element discrepancy coefficients above in the two calibration modes, the same approaches to compensate for those are employed to make the RF chain aligned in the measurement system where the amplitude and the phase compensations are achieved by attenuators and phase shifters, respectively. The attenuation β_n and phase shift γ_n of the n-th element for element amplitude and phase discrepancies compensation are set as, respectively

$$\beta_n = \lfloor \frac{|\alpha_n| - \min\limits_{n' \in [1,N]} |\alpha_{n'}|}{\xi} + \frac{1}{2} \rfloor \xi, \tag{6}$$

$$\gamma_n = \lfloor \frac{\max\limits_{n' \in [1,N]} \angle\alpha_{n'} - \angle\alpha_n}{\mu} + \frac{1}{2} \rfloor \mu, \tag{7}$$

where $|\cdot|$ and $\angle\{\cdot\}$ denote amplitude and phase of a complex number, respectively. $\lfloor \cdot \rfloor$ is a round-down operator. ξ and μ are the minimal step of attenuation and phase shift, respectively.

B. Beam-Steering Pattern

As shown in Fig. 2, the AiP beam-steering is basically performed on two planes defined by xy-axes and xz-axes, i.e. called xy plane and xz plane, respectively in the remaining of the paper. The beam-steering angles relative to x-axis are ϕ and θ for xy-plane and xz-plane steering, respectively, as

$$\phi = \theta = \arcsin \frac{\Delta}{kd}, \tag{8}$$

where Δ is the available phase shift between two adjacent elements in y-axis or z-axis direction. k and d are the wave number and and element spacing, respectively. $\Delta = m\mu$ is set from $-180°$ to $180°$ with a uniform minimal step $\mu = 360°/2^K$, i.e. $2^K + 1$ beam-steering angles $\phi(m)$ or $\theta(m)$ can be performed on each plane as

$$\phi(m) = \theta(m) = \arcsin \frac{m\mu}{kd}, \ m \in [-2^{K-1}, 2^{K-1}]. \tag{9}$$

For the electronic beam-steering angle $\phi(m)$ and $\theta(m)$, the corresponding phase shift $\Phi_n \in [0, 360°)$ of the n-th element for xy-plane and xz-plane steering is set as, respectively

$$\Phi_n^{xy}(m) = \begin{cases} 0 \cdot m\mu, \text{for } n = L + Lh \\ 1 \cdot m\mu \mod 360, \text{for } n = L - 1 + Lh \\ \vdots \\ (L-1) \cdot m\mu \mod 360, \text{for } n = 1 + Lh \end{cases}, \tag{10}$$

$$\Phi_n^{xz}(m) = \begin{cases} 0 \cdot m\mu, \text{for } n = 1 + L(L-1) + h \\ 1 \cdot m\mu \mod 360, \text{for } n = 1 + L(L-2) + h \\ \vdots \\ (L-1) \cdot m\mu \mod 360, \text{for } n = 1 + h \end{cases} \tag{11}$$

where $h \in [0, L-1]$. The operator mod is defined to take the remainder.

Since the AiP is a URA, the beam-steering can be also operated over the space angle $\Omega = \{\theta, \phi\}$ where the desired beam-steering angles θ and ϕ are determined in (9). The steering vector $\boldsymbol{v}(\Omega) = \{v_n(\Omega)\} \in \mathbb{C}^{N\times 1}$ of the AiP array to the desired space angle Ω is expressed as

$$v_n(\Omega) = e^{j\frac{2\pi}{\lambda}\overrightarrow{r_n}\cdot\overrightarrow{\Omega}}, \tag{12}$$

where $\overrightarrow{\Omega} = (\cos\theta\cos\phi, \cos\theta\sin\phi, \sin\theta)$ is a unit vector corresponding to the space angle Ω. $\overrightarrow{r_n} = (0, y_n, z_n)$ is position vector of the n-th AiP element on the yz plane where $y_n = \left[2\left((n-1 \mod L) - \frac{L}{2}\right) + 1\right]d/2$ and $z_n = \left[2\left(\lfloor\frac{n-1}{L}\rfloor - \frac{L}{2}\right) + 1\right]d/2$.

The phase delay $\psi_n(\Omega)$ of the n-th element with respect to the first element can be rewritten as

$$\psi_n(\Omega) = \angle v_n(\Omega) - \angle v_1(\Omega). \tag{13}$$

Therefore, the available phase shift $\Phi_n(\Omega)$ of the n-th element corresponding to the desired beam-steering angle Ω is set as

$$\Phi_n(\Omega) = \lfloor \frac{-\psi_n(\Omega) \mod 360}{\mu} + \frac{1}{2} \rfloor \mu. \tag{14}$$

The radiation pattern $P(\Omega^{'})$ steered towards angle Ω and the corresponding beam-steering pattern $Q(\Omega)$ recording the change of radiation pattern $P(\Omega^{'})$ in the broadside direction of $\Omega^{'} = \{0, 0\}$ can be expressed as, respectively

$$P(\Omega^{'}) = \sum_{n=1}^{N} c_n \cdot e^{j\frac{2\pi}{\lambda}\Phi_n(\Omega)} \cdot v_n(\Omega^{'}), \tag{15}$$

$$Q(\Omega) = \sum_{n=1}^{N} c_n \cdot e^{j\frac{2\pi}{\lambda}\Phi_n(\Omega)}, \tag{16}$$

where $\Omega^{'} = \{\theta^{'}, \phi^{'}\}$ denotes the angles of radiation pattern.

Assuming the isotropic element pattern and identical element excitation (i.e. $c_1 = c_2 \cdots = c_N$), the simulated AiP radiation patterns $P(\phi^{'})$ electronically steered to different angles ϕ on xy plane and the corresponding electronic beam-steering pattern $Q(\phi)$ are shown in Fig. 3(a) and Fig. 3(b), respectively. With the main beam of AiP radiation pattern $P(\phi^{'})$ in Fig. 3(a) steered away from the broadside direction of $\phi = 0°$ (e.g. $\phi > 0°$), the nulls and sidelobes of radiation pattern $P(\phi^{'})$ appear in the broadside direction of AiP in succession. The beam-steering pattern $Q(\phi)$ in Fig. 3(b) records the change of radiation pattern $P(\phi^{'})$ in the broadside direction of $\phi^{'} = 0$ when the radiation pattern $P(\phi^{'})$ is steered towards different beam-steering angles ϕ in Fig. 3(a). With the beam-steering angle ϕ increasing, the beam-steering pattern $Q(\phi)$ drops first (i.e. shift from main beam to null of radiation pattern $P(\phi^{'})$) and then rises (i.e. shift from null to sidelobe of radiation pattern $P(\phi^{'})$), and finally drops again (i.e. shift from sidelobe to another null of radiation pattern $P(\phi^{'})$), as expected. It can be found that the main beam, nulls, and sidelobes of the beam-steering pattern $Q(\phi)$ record the main beam, nulls, and sidelobes of the radiation pattern $P(\phi^{'})$ in the broadside direction in the process of AiP beam-steering, respectively. Therefore, the defined beam-steering pattern $Q(\phi)$ can demonstrate the beam-steering capability of AiP without the need for the radiation pattern $P(\phi^{'})$ measurement.

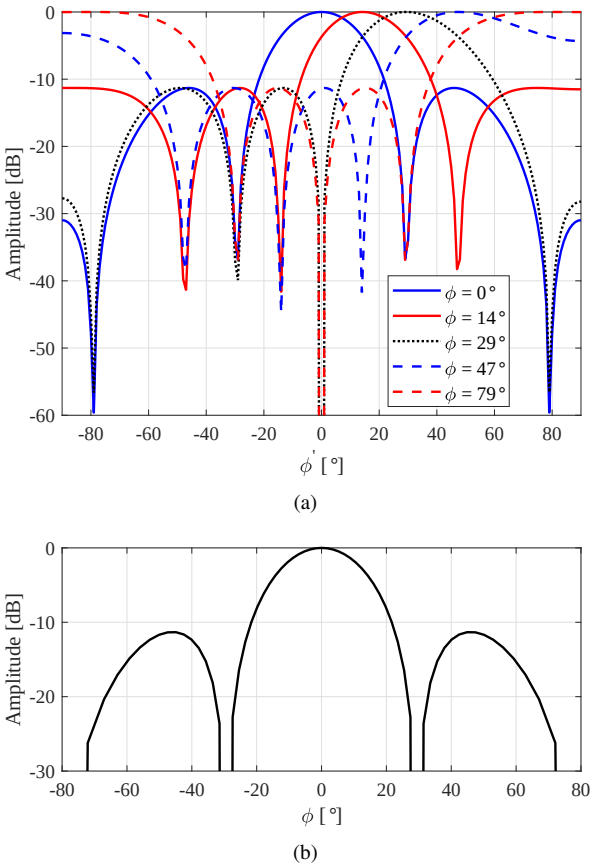

Fig. 3. AiP simulated pattern on xy plane taking $d = 5.45$ mm, $\mu = 5.625°$, and 28 GHz for example. (a) radiation patterns $P(\phi^{'})$ for 5 beam-steering angles ϕ; (b) beam-steering pattern $Q(\phi)$ in this paper.

IV. Experimental Comparison

In accordance with the system model in Section III, a measurement campaign is conducted to experimentally investigate the difference between the on-off and all-on calibration modes for the beam-steering performance of AiP in this section. The measurement results are analyzed and compared following the measurement campaign.

A. Measurement Campaign

The on-off and all-on calibration modes are experimentally compared on a mmWave phased array AiP experimental platform developed at Aalborg University [26]. Fig. 4 shows the experimental setup in an anechoic chamber that consists of

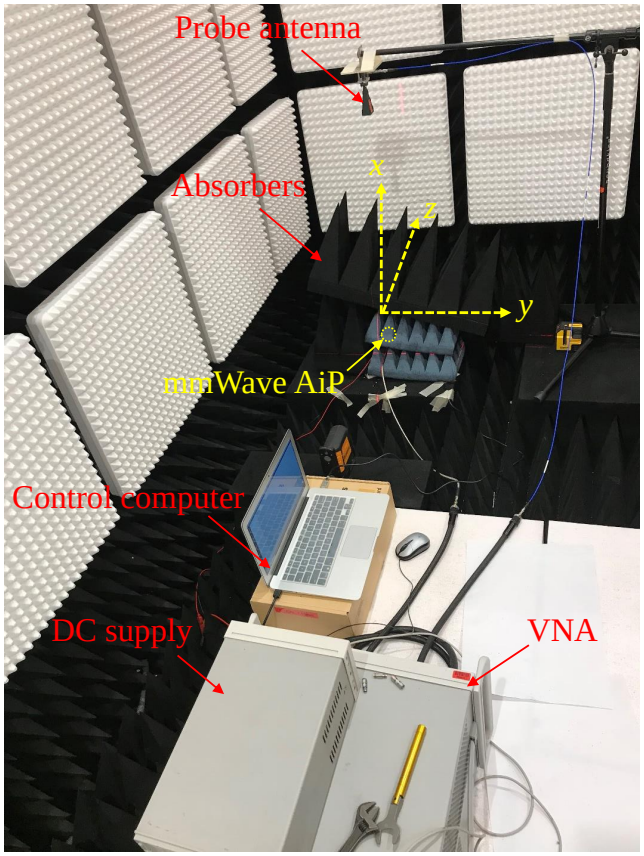

Fig. 4. A photo of experimental setup in an anechoic chamber. Note that the AiP is buried in the absorbers and therefore not seen in the photo.

a mmWave AiP with a DC power supply, a probe antenna (a standard gain horn antenna), a VNA, and a control computer. Operating from 26.5 to 29.5 GHz, the mmWave AiP integrates four AWMF-0158 RF chips and a 4×4 patch array with an element spacing of 5.45 mm (i.e. $L = 4$, $N = 16$, $d = 5.45$ mm). The minimal phase shift and attenuation of phase shifters and attenuators in AiP are 5.625° and 0.5 dB, respectively (i.e. $\mu = 5.625°$ and $\xi = 0.5$ dB). The phase shift, attenuation, and on/off switch of elements can be easily controlled by commands in AiP. The DC power is supplied for the AiP with RF amplifiers inside. The probe antenna is located in the broadside direction of AiP with a distance of 0.73 m larger than the AiP far-field distance of around 0.18 m. With the polarization of probe antenna and AiP aligned, ports 3 and 4 of VNA are connected to the ports of probe antenna and AiP, respectively. The RF cables between each antenna and VNA ports are calibrated out so that the S parameter in Section III is obtained by the measured S_{43} parameter in VNA. 16 and 65×16 measurements of S_{43} are performed for the on-off and all-on calibration measurements, respectively. In the beam-steering measurement, 65×2 and 65×65 measurements of S_{43} are conducted for 2 planes (xy and xz planes) and 3D space steering, respectively. The AiP calibration and beam-steering measurements are automatically conducted with the help of the control computer, which greatly saves time and efforts of measurement campaign (e.g. 65×65 = 4225 automated measurements and data storing only take 30 minutes).

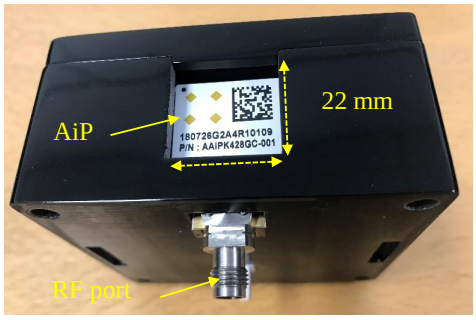

AiP-1

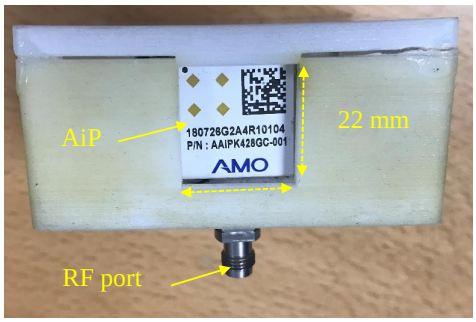

AiP-2

Fig. 5. Photograph of two AiPs in the experiment.

Two AiP samples are investigated in the experiment, as shown in Fig. 5. AiP-1 and AiP-2 are measured at 29.5 GHz and 28 GHz, respectively. The calibration and beam-steering measurements of two AiPs are performed at their respective frequency. For each AiP, the element discrepancies α_n in the on-off and all-on modes are obtained first by the on-off and all-on calibration modes (detailed in Section III-A1 and Section III-A2), respectively. Two beam-steering measurements are then performed in the normal all-on working mode after the compensation for the obtained discrepancies obtained in the on-off and all-on modes, respectively. The settings of attenuation β_n and phase shift γ_n for the discrepancies compensation, and the extra phase shift setting Φ_n for beam-steering are detailed in Section III-A and Section III-B, respectively. In addition, the beam-steering measurement without the compensation for element discrepancies is also performed to demonstrate the effectiveness of AiP calibration. Note that since the compensation for element amplitude discrepancies is implemented by setting element attenuation in practice for both calibration modes, both patterns after compensation behave lower power than the pattern without compensation. The normalized patterns after compensation are compared in the following measurement results.

B. Measurement Results

The element excitation discrepancies α_n of AiP-1 obtained in the on-off and all-on modes are compared in Fig. 6. The obtained element discrepancies are slightly different between the two modes. The amplitude and phase errors between the two modes are ±1 dB and ±8°, respectively. The 3D beam-steering patterns before and after calibration are shown in Fig.

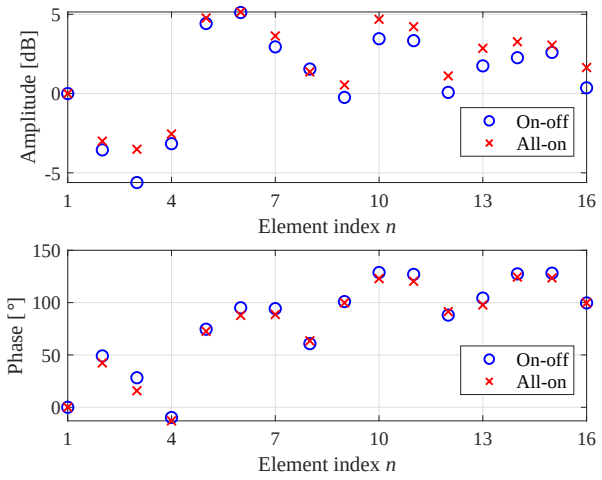

Fig. 6. Element excitation discrepancies of AiP-1 obtained in the two modes.

7. The beam-steering patterns after the two calibration modes are improved compared with pattern before AiP calibration, as expected. Note that the impact of AiP calibration on the beam-steering pattern is explained in [26], which is not the focus in this paper. The focus of this work is on the difference between the two calibration modes. The 3D beam-steering patterns after calibration seem no difference between the two modes. For comparison, beam-steering patterns on xy plane and xz plane after the two calibration modes are shown in Fig. 8. The difference between the two beam-steering patterns on xy or xz plane is little in terms of both main beam and sidelobes area, while the difference is large in the nulls area.

Fig. 9 compares the element discrepancies obtained in the two modes for AiP-2. The element discrepancies of AiP-2 are largely different between the two modes. The amplitude and phase errors between the two modes are $\pm$2.5 dB and $\pm$20°, respectively. Fig. 10 shows the beam-steering patterns after the two calibration modes on two steering planes. In the main beam pattern, there is no difference between the two modes. However, large difference exists in the nulls and sidelobes.

The measurement results show that the on-off and all-on calibration modes of each AiP obtain the same beam-steering performance for the main beam pattern. Since the element branch discrepancies obtained in the two modes are to some extent different, the actual element excitation distribution in the normal all-on mode is somewhat different as well after the compensation for the element discrepancies obtained in the two modes, i.e. two actual element excitation distributions for the two calibration modes. However, the main beam pattern is not sensitive to the element excitation distribution error. Therefore, the same main beam patterns can be observed for the two different element excitation distributions in the all-on working mode.

V. Conclusion

This paper experimentally investigates the difference between the on-off and all-on calibration modes in terms of the obtained element excitation discrepancies for the beam-steering performance of mmWave phased array AiP. Each

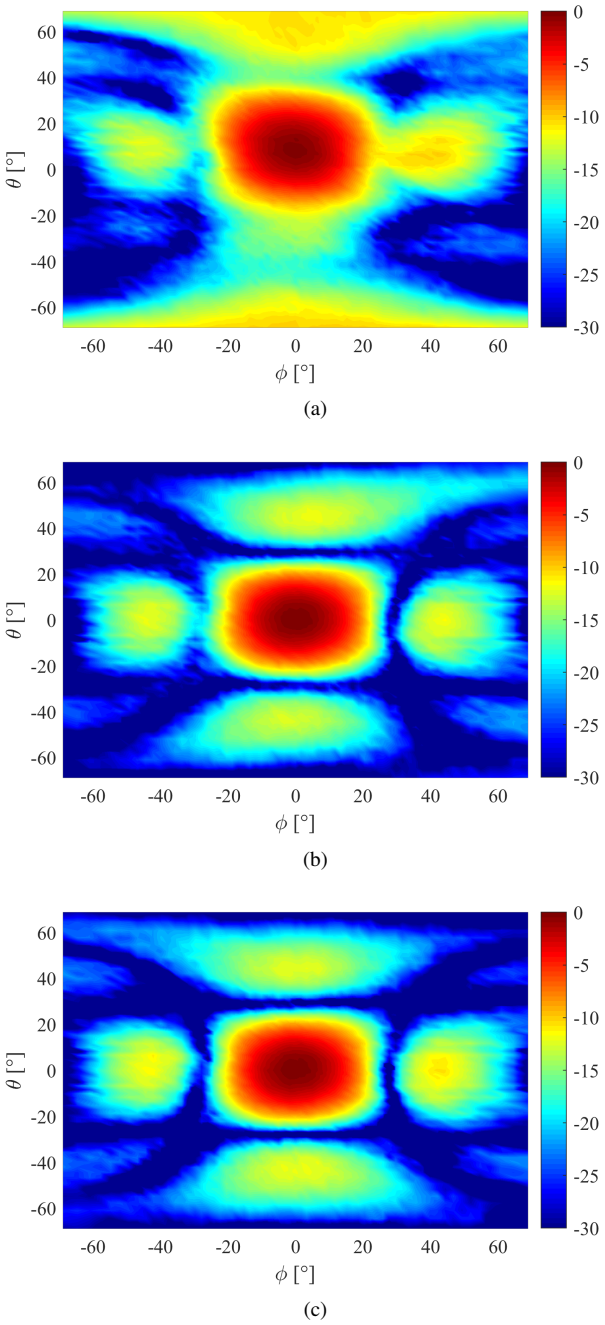

Fig. 7. 3D beam-steering patterns of AiP-1. (a) without calibration; (b) after on-off calibration; (c) after all-on calibration.

calibration mode is to first obtain the element excitation discrepancies in this mode and then to compensate for those for the beam-steering in the normal all-on working mode. The element discrepancies obtained in the two modes might be different in a practical AiP design, e.g. $\pm$1 dB amplitude and $\pm$8° phase difference for AiP-1, while $\pm$2.5 dB and $\pm$20° difference for AiP-2 in our work. When the discrepancies difference is slight, the two calibration modes lead to the same beam-steering performance in the main beam and sidelobes. However, the beam-steering performance is different in terms of both nulls and sidelobes when the discrepancies difference

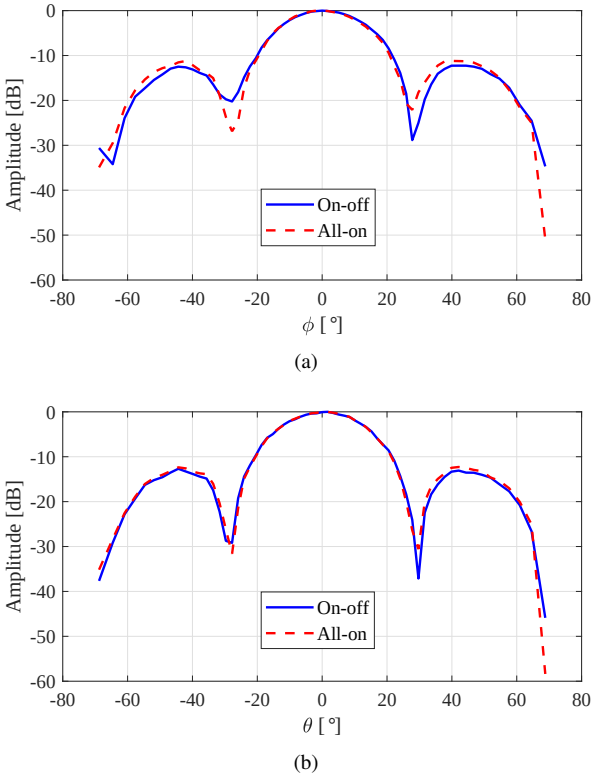

Fig. 8. Beam-steering patterns of AiP-1 on two planes after the two calibration modes. (a) xy plane; (b) xz plane.

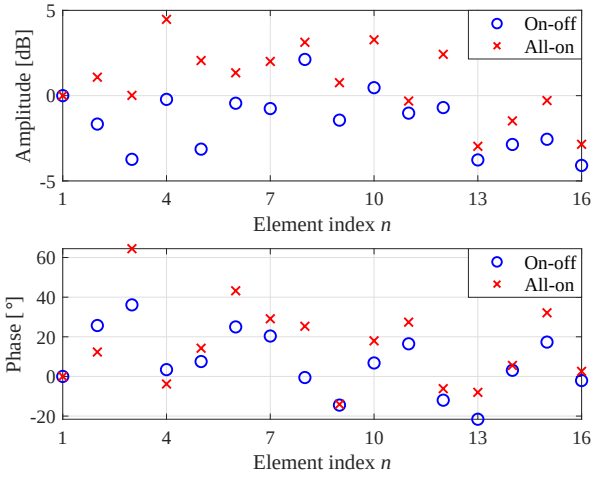

Fig. 9. Element excitation discrepancies of AiP-2 obtained in the two modes.

between the two calibration modes is large. In this case, the two calibration modes bring about the same beam-steering performance only in the main beam pattern. Whether the discrepancies difference between the two calibration modes is small or not, the same beam-steering performance can be obtained after the two calibration modes for the main beam pattern. Therefore, for beam-steering applications where main beam is the focus, e.g. mmWave cellular handset, it does not matter which calibration mode is used. In this case, the conventional on-off calibration mode will not change the

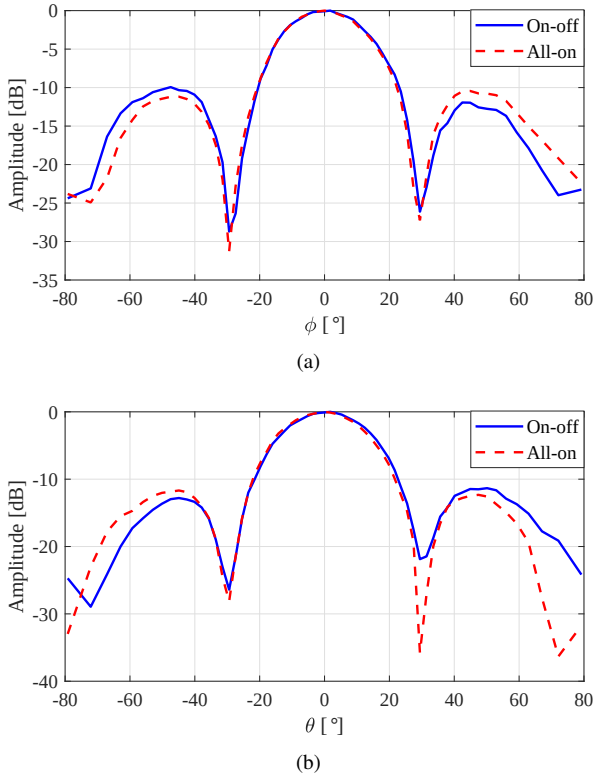

Fig. 10. Beam-steering patterns of AiP-2 on two planes after the two calibration modes. (a) xy plane; (b) xz plane.

beam-steering performance using the all-on calibration mode, though the two calibration modes obtain different excitation discrepancies. However, the difference between the two modes in terms of nulls and side-lobes might be non-negligible for some applications, e.g. mmWave base station. The main reason is that nulls and sidelobes of array pattern are more sensitive to element complex excitations, while main beams are not.

REFERENCES

[1] W. Roh, J.-Y. Seol, J. Park, B. Lee, J. Lee, Y. Kim, J. Cho, K. Cheun, and F. Aryanfar, "Millimeter-wave beamforming as an enabling technology for 5g cellular communications: Theoretical feasibility and prototype results," *IEEE communications magazine*, vol. 52, no. 2, pp. 106–113, 2014.

[2] B. Yang, Z. Yu, R. Zhang, J. Zhou, and W. Hong, "Local oscillator phase shifting and harmonic mixing-based high-precision phased array for 5g millimeter-wave communications," *IEEE Transactions on Microwave Theory and Techniques*, vol. 67, no. 7, pp. 3162–3173, 2019.

[3] Y. Wang, R. Wu, J. Pang, D. You, A. A. Fadila, R. Saengchan, X. Fu, D. Matsumoto, T. Nakamura, R. Kubozoe *et al.*, "A 39-ghz 64-element phased-array transceiver with built-in phase and amplitude calibrations for large-array 5g nr in 65-nm cmos," *IEEE Journal of Solid-State Circuits*, vol. 55, no. 5, pp. 1249–1269, 2020.

[4] M. SeyyedEsfahlan, E. Öztürk, M. Kaynak, and I. Tekin, "77-ghz four-element phased-array radar receiver front end," *IEEE Transactions on Components, Packaging and Manufacturing Technology*, vol. 6, no. 8, pp. 1162–1173, 2016.

[5] J. Xu, W. Hong, H. Zhang, G. Wang, Y. Yu, and Z. H. Jiang, "An array antenna for both long-and medium-range 77 ghz automotive radar applications," *IEEE Transactions on Antennas and Propagation*, vol. 65, no. 12, pp. 7207–7216, 2017.

[6] A. Srivastav, P. Nguyen, M. McConnell, K. A. Loparo, and S. Mandal, "A highly-digital multi-antenna ground-penetrating radar (gpr) system," *IEEE Transactions on Instrumentation and Measurement*, 2020.

[7] Y. Xiao, Y. Xu, H. Sun, X. Xu, and A. Zhou, "A precise real-time delay calibration method for navigation satellite transceiver," *IEEE Transactions on Instrumentation and Measurement*, vol. 65, no. 11, pp. 2578–2586, 2016.

[8] H. Al-Saedi, S. Gigoyan, W. M. Abdel-Wahab, A. Palizban, A. Taeb, A. Ehsandar, E. Nenasheva, and S. Safavi-Naeini, "A low-cost ka-band circularly polarized passive phased-array antenna for mobile satellite applications," *IEEE Transactions on Antennas and Propagation*, vol. 67, no. 1, pp. 221–231, 2018.

[9] S.-M. Moon, S. Yun, I.-B. Yom, and H. L. Lee, "Phased array shaped-beam satellite antenna with boosted-beam control," *IEEE Transactions on Antennas and Propagation*, vol. 67, no. 12, pp. 7633–7636, 2019.

[10] J. Helander, K. Zhao, Z. Ying, and D. Sjöberg, "Performance analysis of millimeter-wave phased array antennas in cellular handsets," *IEEE Antennas and Wireless Propagation Letters*, vol. 15, pp. 504–507, 2015.

[11] Metawave, "Beamsteering Radar for Safe Automated Driving," https://www.metawave.co/spektra

[12] D. Liu, X. Gu, C. W. Baks, and A. Valdes-Garcia, "Antenna-in-package design considerations for ka-band 5g communication applications," *IEEE Transactions on Antennas and Propagation*, vol. 65, no. 12, pp. 6372–6379, 2017.

[13] A. Townley, P. Swirhun, D. Titz, A. Bisognin, F. Gianesello, R. Pilard, C. Luxey, and A. M. Niknejad, "A 94-ghz 4tx–4rx phased-array fmcw radar transceiver with antenna-in-package," *IEEE Journal of Solid-State Circuits*, vol. 52, no. 5, pp. 1245–1259, 2017.

[14] Y. Zhang and J. Mao, "An overview of the development of antenna-in-package technology for highly integrated wireless devices," *Proceedings of the IEEE*, vol. 107, no. 11, pp. 2265–2280, 2019.

[15] J. Park, D. Choi, and W. Hong, "Millimeter-wave phased-array antenna-in-package (aip) using stamped metal process for enhanced heat dissipation," *IEEE Antennas and Wireless Propagation Letters*, vol. 18, no. 11, pp. 2355–2359, 2019.

[16] B. Sadhu, A. Valdes-Garcia, J.-O. Plouchart, H. Ainspan, A. K. Gupta, M. Ferriss, M. Yeck, M. Sanduleanu, X. Gu, C. W. Baks *et al.*, "A 250-mw 60-ghz cmos transceiver soc integrated with a four-element aip providing broad angular link coverage," *IEEE Journal of Solid-State Circuits*, 2019.

[17] I. Şeker, "Calibration methods for phased array radars," in *Radar Sensor Technology XVII*, vol. 8714. International Society for Optics and Photonics, 2013, p. 87140W.

[18] H. Kong, Z. Wen, Y. Jing, and M. Yau, "Midfield over-the-air test: A new ota rf performance test method for 5g massive mimo devices," *IEEE Transactions on Microwave Theory and Techniques*, vol. 67, no. 7, pp. 2873–2883, 2019.

[19] L. Kuai, J. Chen, Z. H. Jiang, C. Yu, C. Guo, Y. Yu, H.-X. Zhou, and W. Hong, "A n260 band 64 channel millimeter wave full-digital multi-beam array for 5g massive mimo applications," *IEEE Access*, vol. 8, pp. 47 640–47 653, 2020.

[20] R. Long, J. Ouyang, F. Yang, W. Han, and L. Zhou, "Fast amplitude-only measurement method for phased array calibration," *IEEE transactions on antennas and propagation*, vol. 65, no. 4, pp. 1815–1822, 2016.

[21] ——, "Multi-element phased array calibration method by solving linear equations," *IEEE Transactions on Antennas and Propagation*, vol. 65, no. 6, pp. 2931–2939, 2017.

[22] F. Zhang, W. Fan, Z. Wang, Y. Zhang, and G. F. Pedersen, "Improved over-the-air phased array calibration based on measured complex array signals," *IEEE Antennas and Wireless Propagation Letters*, vol. 18, no. 6, pp. 1174–1178, 2019.

[23] S. Mano and T. Katagi, "A method for measuring amplitude and phase of each radiating element of a phased array antenna," *Electronics and Communications in Japan (Part I: Communications)*, vol. 65, no. 5, pp. 58–64, 1982.

[24] K.-M. Lee, R.-S. Chu, and S.-C. Liu, "A built-in performance-monitoring/fault isolation and correction (pm/fic) system for active phased-array antennas," *IEEE transactions on antennas and propagation*, vol. 41, no. 11, pp. 1530–1540, 1993.

[25] T. Takahashi, Y. Konishi, and I. Chiba, "A novel amplitude-only measurement method to determine element fields in phased arrays," *IEEE transactions on antennas and propagation*, vol. 60, no. 7, pp. 3222–3230, 2012.

[26] H. Gao, W. Wang, W. Fan, F. Zhang, Z. Wang, Y. Wu, Y. Liu, and G. F. Pedersen, "Design and experimental validation of automated millimeter-wave phased array antenna-in-package (aip) experimental platform," *IEEE Transactions on Instrumentation and Measurement*, vol. 70, pp. 1–11, 2021.

[27] H. Gao, W. Fan, W. Wang, F. Zhang, Z. Wang, Y. Wu, Y. Liu, and G. F. Pedersen, "On uncertainty investigation of mmwave phased array element control with an all-on method," *IEEE Antennas and Wireless Propagation Letters*, vol. 19, no. 11, pp. 1993–1997, 2020.